# Processing and properties of luminescent Cr3+ doped transparent alumina ceramics

DRDLÍKOVÁ, K.; KLEMENT, R.; DRDLÍK, D.; GALUSEK, D.; MACA, K.

Journal of the European Ceramic Society
2018, vol. 40, iss. 7, pp. 2573-2580

ISSN: 0043-1648

DOI: https://doi.org/10.1016/j.jeurceramsoc.2019.11.010

Accepted manuscript

# Processing and properties of luminescent $Cr^{3+}$ doped transparent alumina ceramics

Katarina Drdlikova[a], Robert Klement[b], Daniel Drdlik[a,c], Dušan Galusek[b, d], Karel Maca[a,c]

[a] *CEITEC BUT, Brno University of Technology, Brno, Purkynova 123, Brno 612 00, Czech Republic*

[b] *FunGlass, Alexander Dubček University of Trenčín, Študentská 2, 911 50 Trenčín, Slovak Republic*

[c] *Institute of Materials Science and Engineering, Brno University of Technology, Technicka 2, 616 69 Brno, Czech Republic*

[d] *Joint Glass Centre of the IIC SAS, TnUAD and FChFT STU, Študentská 2, 911 50 Trenčín, Slovak Republic*

**Abstract**

Transparent $Cr_2O_3$-doped alumina ceramics were prepared by slip casting, followed by pre-sintering in ambient atmosphere and hot isostatic pressing. The effect of dopant concentration on material properties, including microstructure and optical properties was evaluated. Real in-line transmittance in the range of 20-44 % was measured for the ceramics with the mean grain size < 520 nm: the transmittance decreased with increasing grain size and Cr content. The excitation spectra consisted of two broad bands with maxima at 404 nm and 558 nm, corresponding to $^4A_{2g} \rightarrow {}^4T_{1g}$ and $^4A_{2g} \rightarrow {}^4T_{2g}$ transitions of $Cr^{3+}$ ions in octahedral sites of $\alpha$-$Al_2O_3$. The intensive deep red narrow emissions under violet/green light excitation, R-lines ($^2E_g \rightarrow {}^4A_{2g}$ transition), were observed at 692.5 nm and 693.8 nm, that are very close to ruby single crystal. The highest emission was achieved at the $Cr^{3+}$ concentration of 0.4 at.%. The

luminescence decay curves exhibited single-exponential behaviour with decay times of ~3.6 ms.

**Keywords**

Alumina; chromium; dopants/doping; luminescence; real in-line transmittance; transparent ceramics

## 1. Introduction

A ruby (Cr: $Al_2O_3$) is not only a gemstone highly valued for centuries, but also the material used in modern technologies such as lasers [1], temperature sensors [2, 3], optoelectronics [4], etc. The exceptional optical, mechanical, thermal and chemical properties of ruby crystals motivate research and development of new materials based on this composition. Numerous studies deal with the preparation of Cr-doped $Al_2O_3$ powders with different crystal structures, e.g. α and γ [5-7] or Cr-doped alumina microspheres [8]. Some attempts aimed at replacement of single crystals with transparent polycrystalline ceramics were also reported [9-11]. Polycrystalline alumina ceramics offers reduced cost and higher variability of shapes and sizes than single crystals. However, the preparation of transparent polycrystalline alumina is difficult due to birefringence of alumina crystals, and requires precise adjustment of all processing steps. Even after thorough optimisation, the transparency of the polycrystalline alumina ceramics probably cannot reach values typical for ruby crystals.

Vacuum sintering [10] or spark plasma sintering (SPS) [9, 11] were successfully applied for preparation of transparent Cr-doped alumina ceramics. However, only Wang et al. [11] provide accurate information on material's transparency, which is strongly related to the Cr content. The significant decrease of the transparency with increasing dopant amount, especially in the visible region, was recorded.

Present work aims at preparation of transparent $Cr^{3+}$-doped alumina with various Cr contents, using a processing chain optimised in our previous work on rare-earth doped aluminas [12-15]. This approach includes slip-casting of colloidal suspensions, pressureless pre-sintering followed by hot isostatic pressing (HIP) and ensures careful homogenisation of initial powders, optimal particles´ arrangement in a green body and eliminates carbon contamination during sintering. Attention is paid to attaining fine grained microstructure with homogenous dopants' distribution. In contrast to rare earth elements doped alumina, where the dopants were

distributed along the grain boundaries due to their low solubility in alumina matrix, dissolution of $Cr^{3+}$ in the alumina matrix is expected [16]. Prepared ceramics are thoroughly characterised in terms of their physical, microstructural and optical properties.

The novelty of the present work lies in the evaluation of the effect of $Cr^{3+}$ content on all studied properties and mainly in tailoring of the optimum dopant concentration for the highest photoluminescent intensity and the transparency.

## 2. Experimental

Chromium doped alumina was prepared from commercial high purity $Al_2O_3$ powder (purity of 99.99%, TM-DAR, Taimei Chemicals Co., Japan) with the primary particle size of ~150 nm and nano-$Cr_2O_3$ powder (purity of 99%, GNM – Getnanomaterials, USA) with the primary particle size of ~60 nm. The content of chromium ranged from 0.10 to 0.75 at.% with respect to $Al_2O_3$. The preparation of the samples was carried out according to the procedure described in detail in our recently published papers [12, 13]. The designation of the samples in this work reflects the content of $Cr^{3+}$; e.g. Cr0.1 means 0.10 at.% of Cr with respect to alumina.

Dried samples (2 days drying under ambient conditions, then 3 h at 60°C) were pre-sintered in air in order to attain closed porosity. The sintering regime consisted of heating the green bodies to a pre-defined temperature (1350 - 1390°C) at a heating rate of 20 °C $min^{-1}$, with the dwell time of 2 min. Afterwards the samples were cooled down at the same rate. Pre-sintered samples were HIP-ed at 1200°C for 3 h in argon atmosphere pressurized to 200 MPa.

Density of pre-sintered samples was estimated according to the Archimedes' principle by double weighing method (EN 623-2) in deionised water and related to the theoretical density of alumina (3.99 g $cm^{-3}$).

A scanning electron microscope Lyra 3 (Tescan, Czech Republic) with integrated a Time-of-Flight Secondary Ion Mass Spectrometry (TOF-SIMS) analyser was used to examine the microstructure and chemical composition of sintered bodies. The mean grain size (MGS) was estimated by the linear intercept method (EN 623-3) using a correction factor of 1.56 [17]. Minimum of 200 grains were measured to obtain statistically robust set of data.

A non-polarized He–Ne laser with a wavelength of 632.8 nm was utilised for determining the real in-line transmittance (RIT) of polished samples. RIT values were measured in at least ten different positions for each sample and they were recalculated to constant thickness of 0.8 mm.

The UV-VIS-NIR spectra (optical transmission spectra) of the polished samples were measured on a Cary 5000 spectrometer (Agilent, USA) in the spectral range of 200-2500 nm. The samples were placed at normal incidence to the beam path. The spectra were obtained at a scan rate of 300 nm/min. The transmission spectra were corrected for the reflection losses that in the case of alumina corresponds to ~ 14 %, and recalculated to the 0.8 mm sample thickness to compare experimental data with literature reported data.

The photoluminescence excitation and emission spectra were recorded using a Fluorolog FL3-21 spectrometer (Horiba, Japan) equipped with the photomultiplier tube R928 detector (Hamamatsu Photonics K. K., Japan) operated in photon counting mode. The Xe-lamp (450 W) was used as an excitation light source, and particular excitation wavelength was spectrally filtered using a double monochromator. To eliminate the second-order diffraction of the radiation source on grating, a cut-off filters were used in all measurements. The luminescence spectra of studied samples presented herein were recorded at room temperature in front face mode (backscattering geometry). The luminescence decay curves were recorded at room temperature with the same instrument using a phosphorescence module of the spectrometer. The same flash Xe-lamp was used as an excitation source.

## 3. Results and discussion

### *3.1 The effect of $Cr^{3+}$ on sintering and microstructure of $Cr^{3+}$-doped alumina*

The preparation of the transparent alumina requires precise adjustment of sintering parameters in order to ensure complete elimination of residual porosity and to inhibit the grain growth. Preliminary experiments with the samples containing 0.1, 0.5 and 0.75 at.% of $Cr^{3+}$ showed that the addition of chromium impaired densification; the effect was more pronounced at higher dopant concentrations (Fig. 1). The temperature required to achieve the state of closed porosity increased slightly with increasing content of $Cr^{3+}$ in the alumina matrix. Based on these preliminary experiments, two pre-sintering temperatures (1380°C and 1390°C) were selected for preparation of samples with closed porosity suitable for HIP. HIP was then performed at 1200°C for 3 h, resulting in transparent ceramics (Fig. 2). The samples were approximately 0.8 mm thick and were placed 10 mm above the background.

Preliminary photoluminescence measurements showed significant concentration quenching for the $Cr^{3+}$ concentration of 0.75 at.%. Therefore, the optical properties of transparent $\alpha$-$Al_2O_3$ polycrystalline ceramics are further discussed only for dopant content ranging between 0.1 and 0.5 at.% $Cr^{3+}$.

The influence of the $Cr^{3+}$ content on the mean grain size of HIP-ed samples is shown in Fig. 3. The MGS of $Cr^{3+}$-doped alumina ranged from 380 nm to 520 nm: the MGS increased with the increasing pre-sintering temperature. The difference ranged between 50-90 nm for a given $Cr^{3+}$ concentration. At identical conditions of pre-sintering, the MGS decreased gradually with increasing content of chromium. These results indicate that $Cr^{3+}$ addition decelerated both densification and grain growth, similarly to e.g. $Y^{3+}$ or $Zr^{4+}$ [18].

The chromium cations have unlimited solubility in an alumina crystal lattice, creating a solid solution in the whole concentration range [16]. However, inclusions or regions enriched by Cr may be formed as the results of insufficient homogeneity or diffusion (due to a short sintering

time) that do not allow ideal redistribution of the dopant atoms [12]. To elucidate this effect, harmful for the transparency, a careful examination of the $Cr^{3+}$ distribution in HIP-ed samples was performed. Some typical positive mode TOF-SIMS spectra of $Cr^{3+}$-doped alumina with images of aluminium and chromium distribution are presented in Fig. 4. The TOF-SIMS mass spectra confirmed the presence of $Cr^{3+}$ in the alumina matrix as is documented in detail in the inset figure with the mass range ranging from m/z 49 to m/z 55. A homogeneous distribution of both aluminium and chromium elements is evident from TOF-SIMS images representing projection of the concentration in the z-axis direction (x and y axes belong to the surface region). Nevertheless, from image of chromium distribution it may appear that Cr atoms are in a higher concentration at the surface of sample. This phenomenon was caused by edge effect, when the enhanced excitation of ions from the surface topography occurred. It can be assumed that the processing parameters and thermal treatment allowed fabrication of alumina ceramics with uniform distribution of $Cr^{3+}$.

### *3.2 Optical properties of $Cr^{3+}$-doped alumina*

#### *3.2.1 Real in-line transmittance*

The real in-line transmittance is a real indicator of the materials´ transparency [19]. The dependence of the RIT (at a wavelength of 632.8 nm) on $Cr^{3+}$ content is shown in Fig. 5. The RIT ranged from 23% to 44% related to the samples with the thickness recalculated to the same value of 0.8 mm. The transparency was affected both by the MGS and the $Cr^{3+}$ content. The RIT decreased with the increasing content of $Cr^{3+}$ and with the increasing MGS, which is always higher after pre-sintering at 1390°C (see Fig. 3). In the range studied the effect of grain size seems to be more significant than the influence of the $Cr^{3+}$ doping. Generally, the RIT values were relatively low comparing to Eu- or Er-doped aluminas prepared in a similar way [12-15]. This decrease is mainly attributed to the absorption of light by $Cr^{3+}$ ions in the alumina

matrix at 632.8 nm (see excitation optical spectra in Fig. 6). This was confirmed also by the luminescence spectra measurements: when the Cr-doped samples were excited at this wavelength (633 nm), relatively low intensity of radiation emitted at 694 nm ($Cr^{3+}$) was observed with the same spectral profile typical for $Cr^{3+}$ emission (see Fig. 7). Despite of the fact, that absorption at that wavelength is quite low the laser light is sufficient to excite the $Cr^{3+}$ ions and partially convert the 632.8 nm red light into deep-red emission with maximum at 694 nm that is dispersed to all directions.

*3.2.2 Optical transmission spectra*

The optical transmission spectra of the studied $Cr^{3+}$-doped transparent alumina with various $Cr^{3+}$ concentrations pre-sintered at 1380°C are shown in Fig. 6a. The transmission spectra exhibit two broad bands with the maxima at 403 nm and 558 nm and one "line" band of low intensity at 694 nm corresponding to absorption of $Cr^{3+}$ ions.

In terms of Tanabe-Sugano energy level diagram that shows the splitting of the $Cr^{3+}$ free ion levels ($d^3$ configuration) in an octahedral crystal field as the ratio of crystal field strength to interelectronic repulsion (measured in $D_q/B$ units), five absorption transitions are possible for the ruby with $Dq/B$ value of 2.8 and $B$ =918 $cm^{-1}$; five absorption lines correspond to $^4A_{2g}(^4F) \rightarrow {}^4T_{1g}(^4F)$, $^4A_{2g}(^4F) \rightarrow {}^2T_{2g}(^2G)$, $^4A_{2g}(^4F) \rightarrow {}^4T_{2g}(^4F)$, $^4A_{2g}(^4F) \rightarrow {}^2T_{1g}(^2G)$, $^4A_{2g}(^4F) \rightarrow {}^2E_g(^2G)$ electronic transitions [20, 21]. Three dominant bands commonly observed in absorption spectra are violet, green and red centred at ~400 nm, 555 nm and 692/694 nm (R-lines). The violet ($^4A_{2g}(^4F) \rightarrow {}^4T_{1g}(^4F)$) and green ($^4A_{2g}(^4F) \rightarrow {}^4T_{2g}(^4F)$) transitions as a spin-allowed transition result in intensive broad absorption bands; the red $^4A_{2g}(^4F) \rightarrow {}^2E_{2g}(^2G)$ is spin-forbidden transition of much lower intensity. The weak spin-forbidden quartet-doublet transitions $^4A_{2g}(^4F) \rightarrow {}^2T_{1g}(^2G)/{}^2T_{1g}(^2G)$ are rarely observed and resolved in the absorption spectra [20-22].

Compared to the alumina single crystal with almost constant transmission (~86%) in the whole visible spectral range, the transmission of prepared transparent polycrystalline $Cr^{3+}$-doped alumina samples decreases with decreasing wavelength due to the scattering of the incident light at grain boundaries, which is wavelength dependent. The transmission of prepared samples was found to be similar to the data published previously on the $Al_2O_3$:$Cr^{3+}$ doped transparent polycrystalline ceramics [11, 22, 23]. Samples pre-sintered at 1390°C exhibit lower transmission compared to the samples pre-sintered at 1380°C because of larger grain size and larger scattering affect. The transmission spectra were corrected for reflection losses, converted into absorbance scale, normalised to 1 cm thickness, and background corrected using the exponential function to eliminate the light scattering effect at grain boundaries. The absorption spectra are shown in Fig. 6b. The absorbance increased with increasing $Cr^{3+}$ concentration and calculated molar absorption coefficients, $\varepsilon$, (using the linear fit according to the Lambert-Beer law $A/l = \varepsilon c$) for violet and green absorption were found to be $3.8\pm0.1\times10^4$ $mol^{-1}cm^2$ (38 $L^{-1}\cdot mol^{-1}cm$) and $2.4\pm0.1\times10^4$ $mol^{-1}cm^2$ (24 $L^{-1}\cdot mol^{-1}cm$), respectively. Almost identical values were found for samples pre-sintered at 1390°C (36 and 24 $L^{-1}\cdot mol^{-1}\cdot cm$). The red absorption was too weak to determine the molar absorption coefficient reliably. Absorption cross-section values, $\sigma$, for violet and green absorption were calculated to be $1.45\times10^{-19}$ $cm^2$ and $9.22\times10^{-20}$ $cm^2$, respectively. These absorption-cross section (ACS) data corresponds quite well with the average ACS data reported by Dodd et al. [24] for ruby single crystal doped with different concentration of $Cr^{3+}$ ions; $1.98\times10^{-19}$ $cm^2$ and $1.20\times10^{-19}$ $cm^2$. Somewhat higher ACS data were reported by Cronemeyer [25] for ruby single crystal. The differences between our data and data reported by Dodd et al. [24] and Cronemeyer [25] are most likely due to sample processing, either caused by Cr lost and/or by partial reduction of $Cr^{3+}$ species to $Cr^{2+}$ [26]. Penilla et al. [22] reported a detailed analysis of transmission spectra of polycrystalline $Al_2O_3$:$Cr^{3+}$ transparent ceramics at $Cr^{3+}$ doping level of 0.5 at.% and 1.0 at.% and grain size

similar to our samples. The applied modified analytical model is based on Rayleigh-Gans-Debye approximation that was already employed for transparent alumina ceramics [19, 27]. The peak absorption coefficients denoted as $\alpha$ (in $cm^{-1}$) of our sample Cr0.5 were around 16.9 $cm^{-1}$ ($\sigma = 1.43\times10^{-19}$ $cm^2$) for violet and 10.4 $cm^{-1}$ ($\sigma = 8.84\times10^{-20}$ $cm^2$) for green absorption and these values are in a good agreement to those reported by Penilla et al. [22] for the same concentration of $Cr^{3+}$ in $Al_2O_3$ polycrystalline transparent ceramics ($\alpha$(violet) = 14.2 $cm^{-1}$ ($\sigma = 1.20\times10^{-19}$ $cm^2$) and $\alpha$(green) = 9.0 $cm^{-1}$ ($\sigma = 7.63\times10^{-20}$ $cm^2$)). The reported grain size is slightly lower (344 nm) compared to the grain size of our sample (380 nm).

*3.2.3 Photoluminescence properties*

The excitation (PLE) spectra of HIPed samples pre-sintered at 1380°C are shown in Fig. 7. The PLE spectra monitored at 694 nm show two intensive broad bands centred at 404 nm (24700 $cm^{-1}$) and 558 nm (17900 $cm^{-1}$) corresponding to the spin-allowed $^4A_{2g}(^4F) \rightarrow {}^4T_{1g}(^4F)$ and $^4A_{2g}(^4F) \rightarrow {}^4T_{2g}(^4F)$ transitions of $Cr^{3+}$ ions in octahedral sites of $\alpha$-$Al_2O_3$ [28-30]. The broad nature of these transitions is a consequence of the character of energy states involved in transitions, that are sensitive to distortion of coordination polyhedra, Cr-O bond length and hence, to the ligand field strength around $Cr^{3+}$ ions. The intensity of the violet absorption is higher than the green one, but with increasing $Cr^{3+}$ concentration the intensity of the green absorption increases. For the concentration of 0.5 at.% $Cr^{3+}$ the intensity ratio, $IR = I(^4T_{1g})/I(^4T_{2g})$, approaches ~1. However in the sample containing 0.75 at.% of $Cr^{3+}$ (spectrum not shown) the value is again reduced to 0.9. The shapes of all spectra are very similar. Similar behaviour was observed also for samples pre-sintered at 1390°C. Analogous effect on PLE intensity ratio was observed by Toyoda et al. [31] for $Cr^{3+}$-doped $Al_2O_3$ ceramic and Murphy et al. [32] for polycrystalline ruby samples. The decrease in *IR* value with increasing $Cr^{3+}$ concentration was discussed in details by Murphy using a rate-equation model and is possibly

due to the increase of non-radiative processes at the $^2E_g(^2G) \rightarrow {}^4A_{2g}(^4F)$ transition, indicating concentration quenching [32]. Two cases observed in PLE spectra of $Cr^{3+}$-doped $Al_2O_3$ prepared via different synthetic routes for both lower and higher $Cr^{3+}$ doping levels were reported in the literature: (*i*) The $IR > 1$ with higher absorption intensity in violet-blue spectral range [29, 33, 34] and (*ii*) $IR < 1$ with higher absorption intensity in green-yellow spectral range [28, 30, 35-40], respectively. According to the Tanabe-Sugano diagram for $Cr^{3+}$ ($d^3$ electron configuration), the $^4T_{1g}$ and $^4T_{2g}$ energy levels are sensitive to the crystal field strength that is affected by $Cr^{3+}$ ions coordination environment. Thus, distortion of the coordination polyhedra around $Cr^{3+}$ ions, interaction with the host lattice and also defects may affect the dynamics of $^2E_g(^2G) \rightarrow {}^4A_{2g}(^4F)$ transition, that is used to monitor light absorption. As a consequence, the method of preparation, sample morphology, and heat treatment may influence the intensity of particular transition in PLE spectra.

The photoluminescence emission (PL) spectra of Cr0.1 under excitation either at 404 nm or 560 nm (see Fig. 8a) exhibited very narrow (with FWHM 23 $cm^{-1}$ and 19 $cm^{-1}$) so-called zero-phonon R-lines (Raman lines $R_1$ and $R_2$) at 692.5 nm (14442 $cm^{-1}$) and 693.8 nm (14412 $cm^{-1}$) assigned to spin-forbidden $^2E_g(^2G) \rightarrow {}^4A_{2g}(^4F)$ transition originating from isolated $Cr^{3+}$ ions in octahedral sites [28-30, 35, 36, 41] as $Cr^{3+}$ ions substitute $Al^{3+}$ ions in the $\alpha$-$Al_2O_3$ lattice. The existence of two R-lines is caused by splitting of the $^2E_g$ excited state that consists of two sublevels, due to spin-orbit coupling. Two observed R-lines, the $R_1$ and $R_2$ lines, are separated by 30 $cm^{-1}$. The R line positions of $Cr^{3+}$ ions in bulk ruby single crystal are 694.3 nm ($R_1$) and 692.9 nm ($R_2$) with separation of 29 $cm^{-1}$ [41, 42]. Thus, the R lines observed in the present work are very close to that of single crystal. The narrow character of the PL emission results from the fact that excited state $^2E_g$ is only slightly influenced by the crystal field strength. The intensity of the PL emission is higher under excitation at 404 nm than at 560 nm for lower $Cr^{3+}$ concentration (see Fig. 8a), however, with increasing concentration the intensities are

comparable and almost identical (for sample containing 0.5 at.% of $Cr^{3+}$) for both excitation wavelengths, as follows from the PLE spectra (see Fig. 8b). The emissions of the much lower intensity (sidebands) were also observed on the Stokes and anti-Stokes side of R-lines at 658, 669, 675, 680, 707, 713 nm. The weak sharp lines called N-lines observed at 699.3, 701.3, 704.2 nm, indicate the presence of Cr-Cr pairs and can be related to emissions of coupled pairs of $Cr^{3+}$ ions, whereas the sidebands, shorter/longer wavelength broader bands around R lines, are associated to phonon assisted transitions due to the electron-phonon coupling in isolated sites [30, 31, 34, 41, 43, 44]. Moreover, the $R_2/R_1$ intensity ratio does not show any correlation with Cr content in the range of studied $Cr^{3+}$ concentrations (normalised PL spectra are almost identical) and is 0.67 (for area $R_2/R_1$ ratios, the value is 0.56). In contrast, the intensity of N-lines increases with increasing Cr content that could be interpreted as a result of growing probability of interactions among neighbouring $Cr^{3+}$ ions.

It is evident that emission intensity strongly depends on doping concentration. The PL intensity increases with increasing $Cr^{3+}$ concentration approaching the maximum at 0.4 at.% (see Fig. 8c,d). At higher chromium concentration the PL intensity decreases due to the concentration quenching as the distance between $Cr^{3+}$-$Cr^{3+}$ ions decreases and energy transfer between the $Cr^{3+}$ ions occurs (becomes more favourable). Based on Dexter´s theory of energy transfer between luminescent species [45, 46], the critical distance between $Cr^{3+}$ ions for energy transfer can be calculated using following equation (1):

$$R_c \approx 2\left[\frac{3V}{4\pi x_c Z}\right]^{1/3} \quad (1)$$

where $V$ is the volume of the unit cell, $x_c$ is the critical concentration of the doping ions and $Z$ is the number of host cations in the unit cell. In case of $\alpha$-$Al_2O_3$, $V$ = 254.7 Å, $Z$ = 12 and the critical concentration of $Cr^{3+}$ ions in $\alpha$-$Al_2O_3$ host is 0.004. The calculated critical distance $R_c$ of $Cr^{3+}$ ions is estimated to be 22 Å. The similar results were obtained for samples pre-sintered at 1390°C. The PL intensities in the spectra recorded using backscattering geometry (front-face

mode) are, however, somewhat higher than for the samples pre-sintered at 1380°C, that is a result of light scattering on samples with lower transparency. The maximum intensity of PL emission was found for concentration 0.4 at.% of $Cr^{3+}$ in $Al_2O_3$ host matrix. The similar optimal $Cr^{3+}$ concentration in $Al_2O_3$ host was reported for ruby crystal (0.15 mol.% $Cr_2O_3$) [28] and for powder $Al_2O_3$:$Cr^{3+}$ phosphors in the range 0.1 at.% up to 1.0 at.% of $Cr^{3+}$ [29, 33, 35, 36].

The crystal field parameters, crystal field strength $D_q$, and Racah parameters $B$ and $C$ can be extracted from experimental excitation and emission spectra using transition energies between the ground state $^4A_{2g}(^4F)$ and states $^4T_{2g}$, $^4T_{1g}$ ($^4F$) and $^2E_g(^2G)$ [20, 47]. The crystal field strength ($D_q$) can be roughly estimated by the peak energy of $^4A_{2g}(^4F) \rightarrow {}^4T_{2g}(^4F)$ transition [20, 47]:

$$D_q = \frac{E(\,^4A_{2g} \rightarrow {}^4T_{2g})}{10} \tag{2}$$

Based on the peak energy difference between $^4A_{2g}(^4F) \rightarrow {}^4T_{1g}(^4F)$ and $^4A_{2g}(^4F) \rightarrow {}^4T_{2g}(^4F)$ transitions, the value of the Racah parameter $B$ can be calculated from the following expressions [20, 47]:

$$\frac{D_q}{B} = \frac{15(x-8)}{(x^2-10x)} \tag{3}$$

where the parameter $x$ is defined as

$$x = \frac{E(\,^4A_{2g} \rightarrow {}^4T_{1g}) - E(\,^4A_{2g} \rightarrow {}^4T_{2g})}{D_q} \tag{4}$$

Finally, according to the peak energy of the emission $^2E_g(^2G) \rightarrow {}^4A_{2g}(^4F)$ transition, the Racah parameter $C$ is evaluated by the equation (5) [20, 47]:

$$E(\,^4A_{2g} \rightarrow {}^2E_g) = 3.05C + 7.08B - \frac{1.8B^2}{D_q} \tag{5}$$

In Tanabe-Sugano diagram for $d^3$ electronic configuration, $^2E_g(^2G)$ energy level is not sensitive to $D_q$ while $^4T_{2g}(^4F)$ varies linearly with crystal field strength. The crossing of the $^2E_g(^2G)$ and $^4T_{2g}(^4F)$ levels occurs near $D_q/B$ value ~2.3 (intermediate crystal field). According to common criterion, when $D_q/B > 2.3$ (strong crystal field), $^2E_g$ level is lower than $^4T_{2g}$ thus resulting in

sharp R-line emission. In weak crystal field $D_q/B < 2.3$, $^4T_{2g}$ energy level is equal or lower than $^2E_g$ level thus broad emission band form $^4T_{2g}$ level to ground state can be observed. In the present work, the crystal field splitting parameter ($D_q$) for $Cr^{3+}$ ion in $\alpha$-$Al_2O_3$ host was found to be 1788 $cm^{-1}$. The calculated Racah *B* parameter is 676 $cm^{-1}$, and $D_q/B$ value of 2.64 indicates that $Cr^{3+}$ ions are positioned in the strong crystal field sites. The nephelauxetic ratio defined as $\beta = B/B_0$ ($B_0$ = 918 $cm^{-1}$ for free $Cr^{3+}$ ion), which is a quantitative measure of the nephelauxetic effect is 0.74. This decrease in *B* value compared to the free ion value is due to partial covalency of Cr-O bond. The Racah parameter *C* is 3304 $cm^{-1}$ ($C_0$ = 3850 $cm^{-1}$ for free $Cr^{3+}$ ion). The similar values of $D_q$ and Racah parameters *B* and *C*, as those for the $Cr^{3+}$ doped transparent alumina ceramics in the present study were found for ruby single crystals and $Al_2O_3$:$Cr^{3+}$ powder phosphors [20, 30, 39].

The competition between the covalence and the ionicity of the chemical bond is the key-factor that determines values of the *B* and *C* parameters. In more covalent hosts, such as oxides, when covalent interaction between the 3d ions and ligand anions is enhanced the *B* and *C* parameters are significantly reduced. The nephelauxetic parameter $\beta$, however, completely ignores the role of the parameter *C*, which is rather crude approximation. Brik et al. [20] suggested to modify this parameter and included also the Racah parameter *C*; $\beta_1 = \sqrt{(B/B_0)^2 + (C/C_0)^2}$. The parameter $\beta_1$ was used to predict the energy of the $^2E_g(^2G) \rightarrow {}^4A_{2g}(^4F)$ transition by applying an empirical linear relation, i.e. $E(^2E_g \rightarrow {}^4A_{2g}) = 3382.80 + 10021.47\ \beta_1$ with the rms deviation of 362 $cm^{-1}$, based on the large number of experimental data of $Cr^{3+}$-doped oxide materials. For $Al_2O_3$:$Cr^{3+}$ studied samples, $\beta_1$ is 1.13, the $^2E_g$ energy position is then calculated as ~ 14700 $cm^{-1}$, the value that is not so far form the experimental value 14412 $cm^{-1}$.

To study the luminescence dynamics, luminescence decay curves of $Al_2O_3$:$Cr^{3+}$ transparent polycrystalline ceramics pre-sintered at 1380°C with different dopant concentrations were

recorded under excitation with pulsed Xe-lamp (see Fig. 9) at room temperature. The samples were excited at 404 nm and emissions were monitored at 694 nm. The PL decay curves can be well fitted with single exponential decay function:

$$I_t = I_0 \exp(-t/\tau), \quad (6)$$

where $I_t$ is the intensity at time $t$, $I_0$ is the intensity at $t = 0$, and $\tau$ is decay lifetime. The fitted fluorescence lifetime values for $Al_2O_3:Cr^{3+}$ transparent ceramics samples are about $3.60 \pm 0.01$ ms and are not significantly affected by the $Cr^{3+}$ concentration in the host matrix within the concentration range up to 0.4 at. % of $Cr^{3+}$. Then, the decay time stars to decrease slightly due to the concentration quenching as also documented by PL intensity decrease at concentrations higher than 0.4 at. % of $Cr^{3+}$ in the $Al_2O_3$ host; for sample containing 0.75 at. % of $Cr^{3+}$ $\tau$ value was found to be $3.52 \pm 0.01$ ms. The values are similar to the value reported in literature of about 3 ms at 300 K for ruby single crystal [42]. The lifetime values for samples pre-sintered at 1390°C were almost identical to lifetime values of samples pre-sintered at 1380°C for particular dopant concentration, so pre-sintering regime had no effect on luminescence dynamics in prepared samples.

## 4. Conclusions

Transparent polycrystalline chromium doped alumina with photoluminescent properties were prepared and characterised in this study. The preparation method consisting of slip casting of fine alumina suspension doped with nano-$Cr_2O_3$ followed by pre-sintering under ambient conditions and hot isostatic pressing at 200 MPa of argon was found to be successful in preparation of transparent $Cr^{3+}$ doped alumina. The optical transmittance and the real in-line transmittance are strongly related to the grain size: proper adjustment of sintering conditions limiting the grain growth is crucial for achieving the transparency. Even mild grain size increase results in the significant transparency decrease. The effect of chromium concentration on the transmittance and RIT in examined range is less pronounced, and only a slight influence was observed in the wavelength region where the light is absorbed by $Cr^{3+}$ dopant ions. The UV-VIS-NIR transmission spectra exhibit two broad bands with the maxima at 403 nm and 558 nm and one "line" band of low intensity at 694 nm corresponding to absorption of $Cr^{3+}$ ions. The absorbance increases with increasing $Cr^{3+}$ concentration in the samples and calculated molar absorption coefficients (using the linear fit) for violet and green absorption were found to be $3.8\times10^4$ $mol^{-1}cm^2$ (38 $L^{-1}mol^{-1}cm$) and $2.4\times10^4$ $mol^{-1}cm^2$ (24 $L^{-1}mol^{-1}cm$), respectively. Almost identical values were found for samples pre-sintered at 1390°C (36 and 24 $L^{-1}mol^{-1}cm$). Absorption cross-section values, $\sigma$, for violet and green absorption were calculated to be $1.45\times10^{-19}$ $cm^2$ and $9.22\times10^{-20}$ $cm^2$, respectively. These data are in a good agreement with values reported either for ruby single crystals or for polycrystalline $Cr^{3+}$- doped alumina. The excitation spectra consist of two broad bands with maxima at 404 nm and 558 nm, corresponding to $^4A_{2g} \rightarrow {}^4T_{1g}$ and $^4A_{2g} \rightarrow {}^4T_{2g}$ transitions of $Cr^{3+}$ ions in octahedral sites of $\alpha$-$Al_2O_3$, and with intensity ratio dependent on the $Cr^{3+}$ concentration. The intensive deep red narrow emissions under violet/green light excitation, R-lines ($^2E_g \rightarrow {}^4A_{2g}$ transition), were observed at 692.5 and 693.8 nm, that are very close to ruby single crystal. The optimal $Cr^{3+}$

doping concentration was found to be 0.4 at.%, with the critical distance between $Cr^{3+}$ ions for energy transfer (concentration quenching), based on Dexter´s theory, of 22 Å. The $D_q/B$ parameter value of 2.64 indicates that $Cr^{3+}$ ions are positioned in the strong crystal field sites. The calculated Racah parameter B was found to be 676 $cm^{-1}$ and parameter C is 3304 $cm^{-1}$. The reduction in the values of Racah parameters compared to the values of free $Cr^{3+}$ ions is due to partial covalency of Cr-O bond. The luminescence decay curves exhibit single-exponential behaviour with decay times of ~3.6 ms, similar to ruby monocrystal, and decay is only slightly affected by the $Cr^{3+}$ concentration.

**Acknowledgements**

This work is part of the project 5SA14857, which has acquired the financial contribution from the EU Framework Programme for Research and Innovation Horizon 2020 within the scope of the Marie Sklodowska-Curie Actions co-financed by the South Moravian Region according to the Grant Agreement no. 665860. The research has also been financially supported by the Ministry of Education, Youth and Sports of the Czech Republic under the projects LTT18013 and CEITEC 2020 (LQ1601). This work was also supported by the Slovak Research and Development Agency under the contract No. APVV-17-0049 and by grant VEGA 1/0527/18. This paper is a part of dissemination activities of the project FunGlass. This project has received funding from the European Union´s Horizon 2020 research and innovation programme under grant agreement No 739566. The authors thank to CEITEC Nano RI, MEYS CR, 2016–2019 for allowing the SEM analyses.

**Figure captions**

Fig. 1 Dependence of relative density of pre-sintered samples on the temperature.

Fig. 2 The photo of HIP-ed samples. The samples are placed 5 mm above the surface.

Fig. 3 Dependence of mean grain size on $Cr^{3+}$ content in alumina ceramics after HIP.

Fig. 4 Positive mode TOF-SIMS mass spectrum in the mass range from m/z 20 to m/z 100 with detail in the mass range from m/z 49 to m/z 55 of the sample containing 0.5 at.% of $Cr^{3+}$pre-sintered at 1380°C after HIP; and TOF-SIMS images of $Al^{+}$ and $Cr^{+}$ distribution.

Fig. 5 Dependence of RIT on the $Cr^{3+}$ content in alumina ceramics.

Fig. 6 Transmission spectra of polycrystalline $Cr^{3+}$-doped alumina transparent ceramic samples prepared using pre-sintering regime 1380°C/2min and HIP 1200°C/3h (a). Inset represents enlarged area of the $Cr^{3+}$ absorptions in spectral range from 200 nm to 800 nm. All data are recalculated to sample thickness of 0.8 mm for comparison. (b) Absorption spectra of polycrystalline doped transparent alumina.

Fig. 7 Excitation spectra of $Cr^{3+}$-doped alumina transparent ceramic samples prepared using pre-sintering regime 1380°C/2min and HIP 1200°C/3h, $\lambda_{mon}$ = 694 nm.

Fig. 8 Emission spectra of the $Al_2O_3$:$Cr^{3+}$ transparent ceramics prepared using pre-sintering regime 1380°C/2min and HIP 1200°C/3h: (a) sample containing 0.1 at.% of $Cr^{3+}$ under excitation by violet (404 nm) and green (560 nm) light; (b, c) emission spectra $Al_2O_3$ ceramics with different concentration of $Cr^{3+}$ (0.1 – 0.5 at.%) in host matrix under excitation at 404 nm. Inset represents enlarged area of low intensity N-lines and sidebands in the spectral range from 650 nm to 740 nm. (d) PL integrated intensity as a function of $Cr^{3+}$ concentration.

Fig. 9 The decay curves of the $Al_2O_3$:$Cr^{3+}$ transparent ceramics with different concentration of $Cr^{3+}$ (0.1 – 0.5 at.%).

**References**

[1] T.H. Maiman, Stimulated optical radiation in ruby, Nature 187 (1960) 493-494. https://doi.org/10.1038/187493a0

[2] K.T.V. Grattan, R.K. Selli, A.W. Palmer, Ruby decay-time fluorescence thermometer in a fiber-optic configuration, Rev Sci Instrum 59 (1988) 1328-1335. https://doi.org/10.1063/1.1140257

[3] H.C. Seat, J.H. Sharp, Z.Y. Zhang, K.T.V. Grattan, Single-crystal ruby fiber temperature sensor, Sensor Actuat a-Phys 101 (2002) 24-29. https://doi.org/10.1016/S0924-4247(02)00190-5

[4] H. Aizawa, N. Ohishi, S. Ogawa, A. Endo, A. Hakamada, T. Katsumata, S. Komuro, T. Morikawa, E. Toba, Characteristics of sapphire fiber connected with ruby sensor head for the fiber-optic thermometer applications, Sensor Actuat a-Phys 101 (2002) 42-48. https://doi.org/10.1016/S0924-4247(02)00148-6

[5] G. Salek, A. Devoti, E. Lataste, A. Demourgues, A. Garcia, V. Jubera, M. Gaudon, Optical properties versus temperature of Cr-doped gamma- and alpha-$Al_2O_3$: Irreversible thermal sensors application, J Lumin 179 (2016) 189-196. https://doi.org/10.1016/j.jlumin.2016.07.004

[6] Y.-L. Zhu, S. Liu, X.-K. Zhang, Y. Xiang, Effects of $Cr^{3+}$ concentration on the crystallinity and optical properties of Cr-doped $Al_2O_3$ powders by solid-state reaction method, IOP Conference Series: Mat Sci Eng 382 (2018) 022037. https://doi.org/10.1088/1757-899X/382/2/022037

[7] M. Ahmed, A. Salah, A. Ashour, H. Hafez, N. El-Faramawy, Dosimetric properties of Cr doped $Al_2O_3$ nanophosphors, J Lumin 196 (2018) 449-454. https://doi.org/10.1016/j.jlumin.2018.01.001

[8] Z.F. Zhu, D.G. Liu, H. Liu, J. Du, H.G. Yu, J. Deng, Fabrication and luminescent properties of $Al_2O_3:Cr^{3+}$ microspheres via a microwave solvothermal route followed by heat treatment, Opt Commun 285 (2012) 3140-3142. https://doi.org/10.1016/j.optcom.2012.02.084

[9] K.Q. Dang, S. Takei, M. Kawahara, M. Nanko, Pulsed electric current sintering of transparent Cr-doped $Al_2O_3$, Ceram Int 37 (2011) 957-963. https://doi.org/10.1016/j.ceramint.2010.11.009

[10] Q. Liu, Q.H. Yang, G.G. Zhao, S.Z. Lu, H.J. Zhang, The thermoluminescence and optically stimulated luminescence properties of Cr-doped alpha alumina transparent ceramics, J Alloy Compd 579 (2013) 259-262. https://doi.org/10.1016/j.jallcom.2013.06.070

[11] C. Wang, Z. Zhao, Transparent polycrystalline ruby ceramic by spark plasma sintering, Mater Res Bull 45 (2010) 1127-1131. https://doi.org/10.1016/j.materresbull.2010.05.034

[12] K. Bodisova, R. Klement, D. Galusek, V. Pouchly, D. Drdlik, K. Maca, Luminescent rare-earth-doped transparent alumina ceramics, J Eur Ceram Soc 36 (2016) 2975-2980. https://doi.org/10.1016/j.jeurceramsoc.2015.12.032

[13] K. Drdlikova, R. Klement, D. Drdlik, T. Spusta, D. Galusek, K. Maca, Luminescent $Er^{3+}$ doped transparent alumina ceramics, J Eur Ceram Soc 37 (2017) 2695-2703. https://doi.org/10.1016/j.jeurceramsoc.2017.02.017

[14] K. Drdlikova, R. Klement, H. Hadraba, D. Drdlik, D. Galusek, K. Maca, Luminescent $Eu^{3+}$-doped transparent alumina ceramics with high hardness, J Eur Ceram Soc 37 (2017) 4271-4277. 10.1016/j.jeurceramsoc.2017.05.007

[15] D. Drdlik, K. Drdlikova, H. Hadraba, K. Maca, Optical, mechanical and fractographic response of transparent alumina ceramics on erbium doping, J Eur Ceram Soc 37 (2017) 4265-4270. https://doi.org/10.1016/j.jeurceramsoc.2017.02.043

[16] Y.K. Ahn, J.G. Seo, J.W. Park, Diffusion of chromium in sapphire: The effects of electron beam irradiation, J Cryst Growth 326 (2011) 45-49. https://doi.org/10.1016/j.jcrysgro.2011.01.049

[17] M.I. Mendelson, Average grain size in polycrystalline ceramics, J Am Ceram Soc 52 (1969) 443-446. https://doi.org/10.1111/j.1151-2916.1969.tb11975.x

[18] K. Maca, V. Pouchly, K. Bodisova, P. Svancarek, D. Galusek, Densification of fine-grained alumina ceramics doped by magnesia, yttria and zirconia evaluated by two different sintering models, J Eur Ceram Soc 34 (2014) 4363-4372. https://doi.org/10.1016/j.jeurceramsoc.2014.06.030

[19] R. Apetz, M.P.B. van Bruggen, Transparent alumina: A light-scattering model, J Am Ceram Soc 52 86 (2003) 480-486. https://doi.org/10.1111/j.1151-2916.2003.tb03325.x

[20] M.G. Brik, S.J. Camardello, A.M. Srivastava, N.M. Avram, A. Suchocki, Spin-forbidden transitions in the spectra of transition metal ions and nephelauxetic effect, Ecs J Solid State Sc 5 (2016) R3067-R3077. https://doi.org/10.1149/2.0091601jss

[21] M.O.J.Y. Hunault, Y. Harada, J. Miyawaki, J. Wang, A. Meijerink, F.M.F. de Groot, M.M. van Schooneveld, Direct observation of $Cr^{3+}$ 3d states in ruby: Toward experimental mechanistic evidence of metal chemistry, J Phys Chem A 122 (2018) 4399-4413. https://doi.org/10.1021/acs.jpca.8b00984

[22] E.H. Penilla, C.L. Hardin, Y. Kodera, S.A. Basun, D.R. Evans, J.E. Garay, The role of scattering and absorption on the optical properties of birefringent polycrystalline ceramics: Modeling and experiments on ruby ($Cr:Al_2O_3$), J Appl Phys 119 (2016) 023106. https://doi.org/10.1063/1.4939090

[23] T. Kato, N. Kawano, G. Okada, N. Kawaguchi, T. Yanagida, Comparative study of dosimeter properties between $Al_2O_3$ transparent ceramic and single crystal, Radiat Meas 107 (2017) 43-47. https://doi.org/10.1016/j.radmeas.2017.09.006

[24] D.M. Dodd, D.L. Wood, R.L. Barns, Spectrophotometric determination of chromium concentration in ruby, J Appl Phys 35 (1964) 1183-1186. https://doi.org/10.1063/1.1713590

[25] D.C. Cronemeyer, Optical absorption characteristics of pink ruby, J Opt Soc Am 56 (1966) 1703-1705. https://doi.org/10.1364/JOSA.56.001703

[26] S. Ganschow, D. Klimm, R. Bertram, On the effect of oxygen partial pressure on the chromium distribution coefficient in melt-grown ruby crystals, J Cryst Growth 325 (2011) 81-84. https://doi.org/10.1016/j.jcrysgro.2011.04.033

[27] C. Pecharroman, G. Mata-Osoro, L.A. Diaz, R. Torrecillas, J.S. Moya, On the transparency of nanostructured alumina: Rayleigh-Gans model for anisotropic spheres, Opt Express 17 (2009) 6899-6912. https://doi.org/10.1364/OE.17.006899

[28] F. Liu, B.A. Goodman, X. Tan, X. Wang, D. Chen, W. Deng, Luminescence and EPR properties of high quality ruby crystals prepared by the optical floating zone method, Opt Mater 91 (2019) 183-188. https://doi.org/10.1016/j.optmat.2019.03.018

[29] D.G. Liu, Effects of Cr content and morphology on the luminescence properties of the Cr-doped alpha-$Al_2O_3$ powders, Ceram Int 39 (2013) 4765-4769. https://doi.org/10.1016/j.ceramint.2012.11.063

[30] V. Singh, R.P.S. Chakradhar, J.L. Rao, K. Al-Shamery, M. Haase, Y.D. Jho, Electron paramagnetic resonance and photoluminescence properties of alpha-$Al_2O_3$:$Cr^{3+}$ phosphors, Appl Phys B 107 (2012) 489-495. https://doi.org/10.1007/s00340-012-4993-x

[31] T. Toyoda, T. Obikawa, T. Shigenari, Photoluminescence spectroscopy of $Cr^{3+}$ in ceramic $Al_2O_3$, Mat Sci Eng B-Solid 54(1-2) (1998) 33-37. https://doi.org/10.1016/S0921-5107(98)00122-6

[32] J.C. Murphy, L.C. Aamodt, Photoacoustic spectroscopy of luminescent solids: Ruby, J Appl Phys 48(8) (1977) 3502-3509. https://doi.org/10.1063/1.324199

[33] D.G. Liu, Z.F. Zhu, H. Liu, Z.Y. Zhang, Y.B. Zhang, G.G. Li, $Al_2O_3$:$Cr^{3+}$ microfibers by hydrothermal route: Luminescence properties, Mater Res Bull 47 (2012) 2332-2335. https://doi.org/10.1016/j.materresbull.2012.05.026

[34] J.M.A. Caiut, N. Floch, Y. Messaddeq, O.J. de Lima, L.A. Rocha, K.J. Ciuffi, E.J. Nassar, G.R. Friedermann, S.J.L. Ribeiro, $Cr^{3+}$ doped $Al_2O_3$ obtained by non-hydrolytic sol-gel methodology, J Braz Chem Soc 30 (2019) 744-751. http://dx.doi.org/10.21577/0103-5053.20180195

[35] G. Rani, P.D. Sahare, Structural and photoluminescent properties of $Al_2O_3$: $Cr^{3+}$ nanoparticles via solution combustion synthesis method, Adv Powder Technol 25 (2014) 767-772. https://doi.org/10.1016/j.apt.2013.11.009

[36] B.N. Han, Y.M. Yang, J.H. Wu, J. Wei, Z.Q. Li, Y.H. Mai, $Al_2O_3$:$Cr^{3+}$/tellurite glass composites: An efficient light converter for silicon solar cell, Ceram Int 41 (2015) 12267-12272. https://doi.org/10.1016/j.ceramint.2015.06.050

[37] J. Ueda, S. Tanabe, Preparation and optical property of glass ceramics containing ruby crystals, J Am Ceram Soc 93 (2010) 3084-3087. https://doi.org/10.1111/j.1551-2916.2010.04065.x

[38] L. Shen, C.F. Hu, S.H. Zhou, A. Mukherjee, Q. Huang, Phase-dependent photoluminescence behavior of Cr-doped alumina phosphors, Opt Mater 35 (2013) 1268-1272. https://doi.org/10.1016/j.optmat.2013.01.022

[39] A. Rastorguev, M. Baronskiy, A. Zhuzhgov, A. Kostyukov, O. Krivoruchko, V. Snytnikov, Local structure of low-temperature gamma-$Al_2O_3$ phases as determined by the luminescence of $Cr^{3+}$ and $Fe^{3+}$, Rsc Adv 5 (2015) 5686-5694. https://doi.org/10.1039/C4RA14524K

[40] A. Kostyukov, M. Baronskiy, A. Rastorguev, V. Snytnikov, V. Snytnikov, A. Zhuzhgov, A. Ishchenko, Photoluminescence of $Cr^{3+}$ in nanostructured $Al_2O_3$ synthesized by evaporation using a continuous wave $CO_2$ laser, Rsc Adv 6 (2016) 2072-2078. https://doi.org/10.1039/C5RA19455E

[41] C. Guguschev, J. Götze, M. Göbbels, Cathodoluminescence microscopy and spectroscopy of synthetic ruby crystals grown by the optical floating zone technique, Am Mineral 95 (2010) 449-455. https://doi.org/10.2138/am.2010.3291

[42] T.H. Maiman, R.H. Hoskins, I.J. D'Haenens, C.K. Asawa, V. Evtuhov, Stimulated optical emission in fluorescent solids. II. Spectroscopy and stimulated emission in ruby, Phys Rev 123 (1961) 1151-1157. https://doi.org/10.1103/PhysRev.123.1151

[43] B. Bondzior, N. Miniajluk, P.J. Deren, Pair luminescence in $Cr^{3+}$-doped $Ba_2Mg(BO_3)_2$, Opt Mater 79 (2018) 269-272. https://doi.org/10.1016/j.optmat.2018.03.028

[44] A.P. Vink, A. Meijerink, Electron-phonon coupling of $Cr^{3+}$-pairs and isolated sites in alpha-$Al_2O_3$ and MgO, Spectrochim Acta A 54 (1998) 1755-1761. https://doi.org/10.1016/S1386-1425(98)00108-5

[45] G. Blasse, Energy transfer in oxidic phosphors, Phys Lett A 28 (1968) 444-445. https://doi.org/10.1016/0375-9601(68)90486-6

[46] G. Blasse, Energy transfer in oxidic phosphors, Philips Research Reports 24 (1969) 131-144.

[47] B. Henderson, G.F. Imbusch, Optical spectroscopy of inorganic solids, Clarendon Press; Oxford University Press, Oxford [Oxfordshire]; New York, 1989.

Figure 1

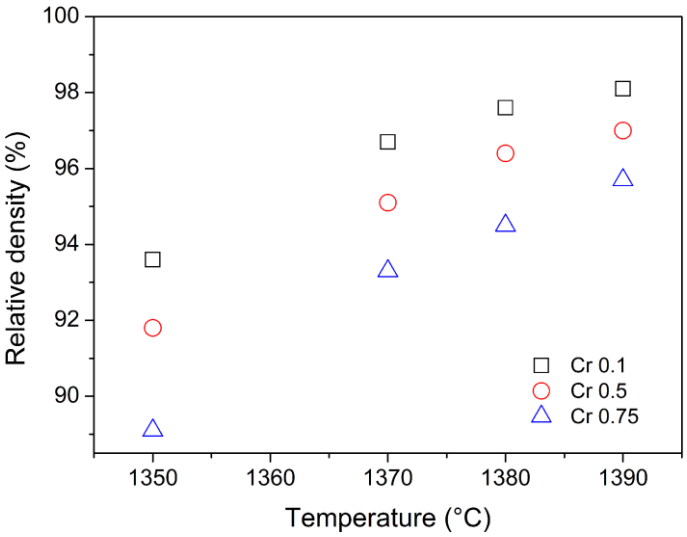
100
98
96
94
92
90
Relative density (%)
1350
1360
1370
1380
1390
Temperature (°C)
Cr 0.1
Cr 0.5
Cr 0.75

Figure 2

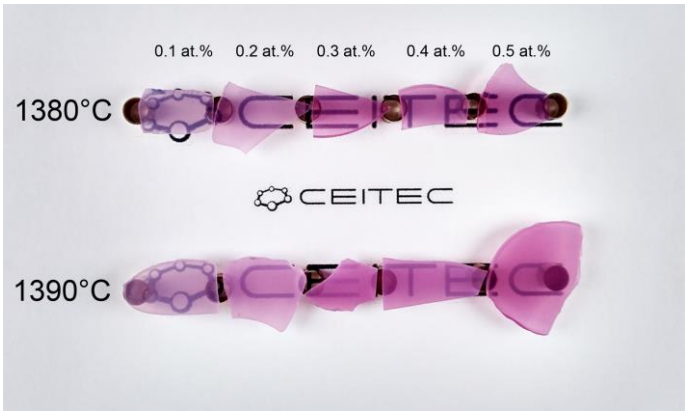

Figure 3

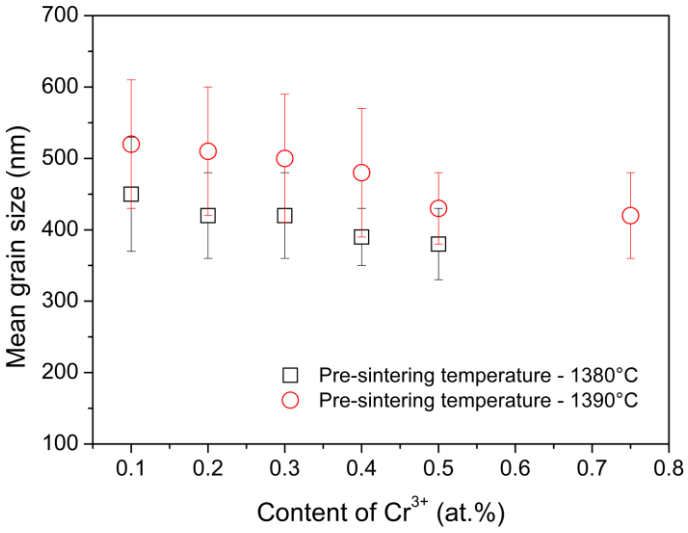
Mean grain size (nm)
700
600
500
400
300
200
100
0.1
0.2
0.3
0.4
0.5
0.6
0.7
0.8
Content of Cr3+ (at.%)
Pre-sintering temperature - 1380°C
Pre-sintering temperature - 1390°C

Figure 4

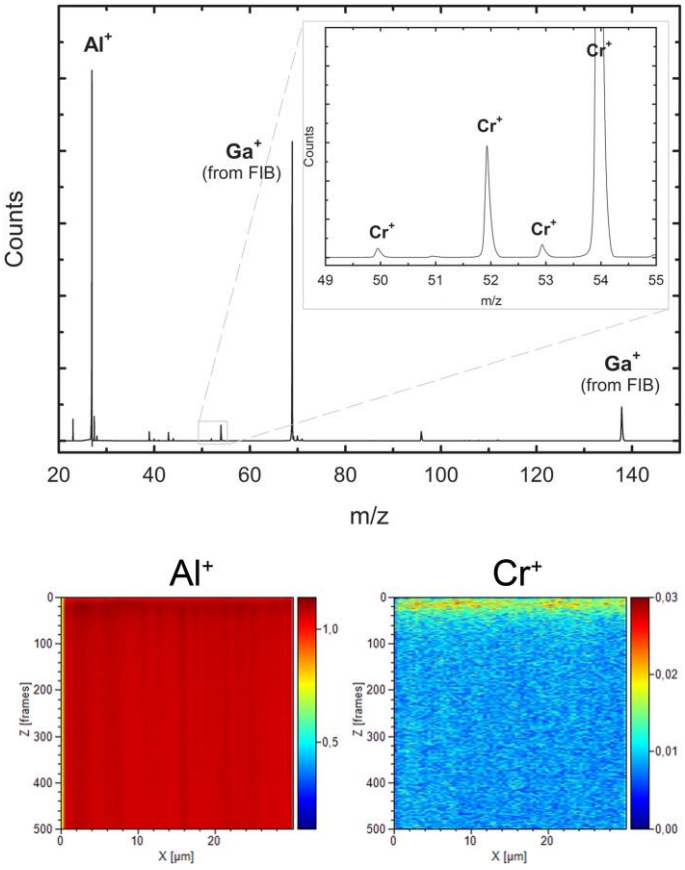
Al+
Ga+
(from FIB)
Counts
Cr+
Cr+
Cr+
Cr+
Counts
49
50
51
52
53
54
55
m/z
Ga+
(from FIB)
20
40
60
80
100
120
140
m/z
Al+
Cr+
Z [frames]
X [µm]
1,0
0,5
0,03
0,02
0,01
0,00

Figure 5

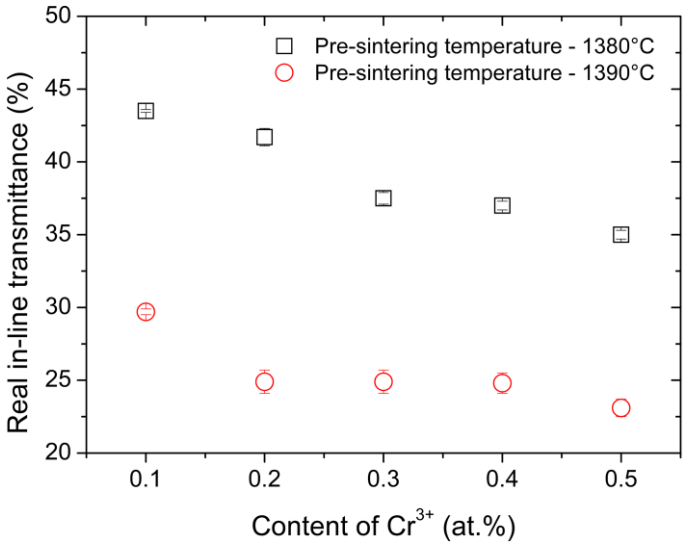
Pre-sintering temperature - 1380°C
Pre-sintering temperature - 1390°C
Real in-line transmittance (%)
Content of Cr3+ (at.%)
50
45
40
35
30
25
20
0.1
0.2
0.3
0.4
0.5

Figure 6

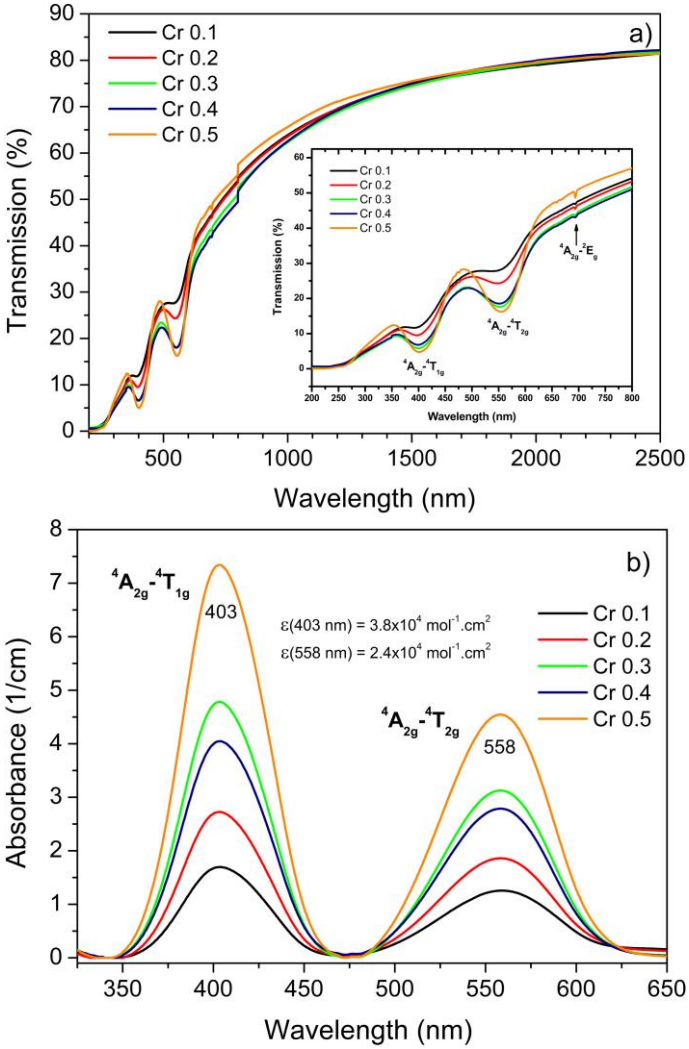
a)
Cr 0.1
Cr 0.2
Cr 0.3
Cr 0.4
Cr 0.5
Transmission (%)
Wavelength (nm)
$^4A_{2g}$-$^4T_{1g}$
$^4A_{2g}$-$^4T_{2g}$
$^4A_{2g}$-$^2E_g$
b)
$^4A_{2g}$-$^4T_{1g}$
403
ε(403 nm) = 3.8x10$^4$ mol$^{-1}$.cm$^2$
ε(558 nm) = 2.4x10$^4$ mol$^{-1}$.cm$^2$
$^4A_{2g}$-$^4T_{2g}$
558
Absorbance (1/cm)
Wavelength (nm)

Figure 7

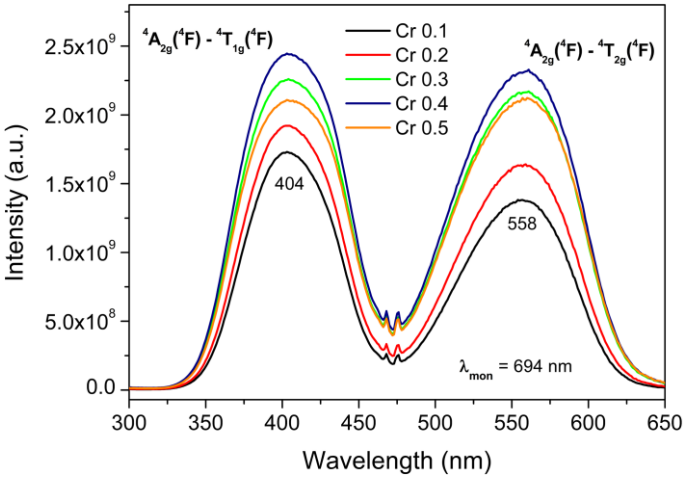
$^4A_{2g}(^4F) - ^4T_{1g}(^4F)$
$^4A_{2g}(^4F) - ^4T_{2g}(^4F)$
Cr 0.1
Cr 0.2
Cr 0.3
Cr 0.4
Cr 0.5
404
558
$\lambda_{mon}$ = 694 nm
Intensity (a.u.)
Wavelength (nm)
2.5x10^9
2.0x10^9
1.5x10^9
1.0x10^9
5.0x10^8
0.0
300
350
400
450
500
550
600
650

Figure 8

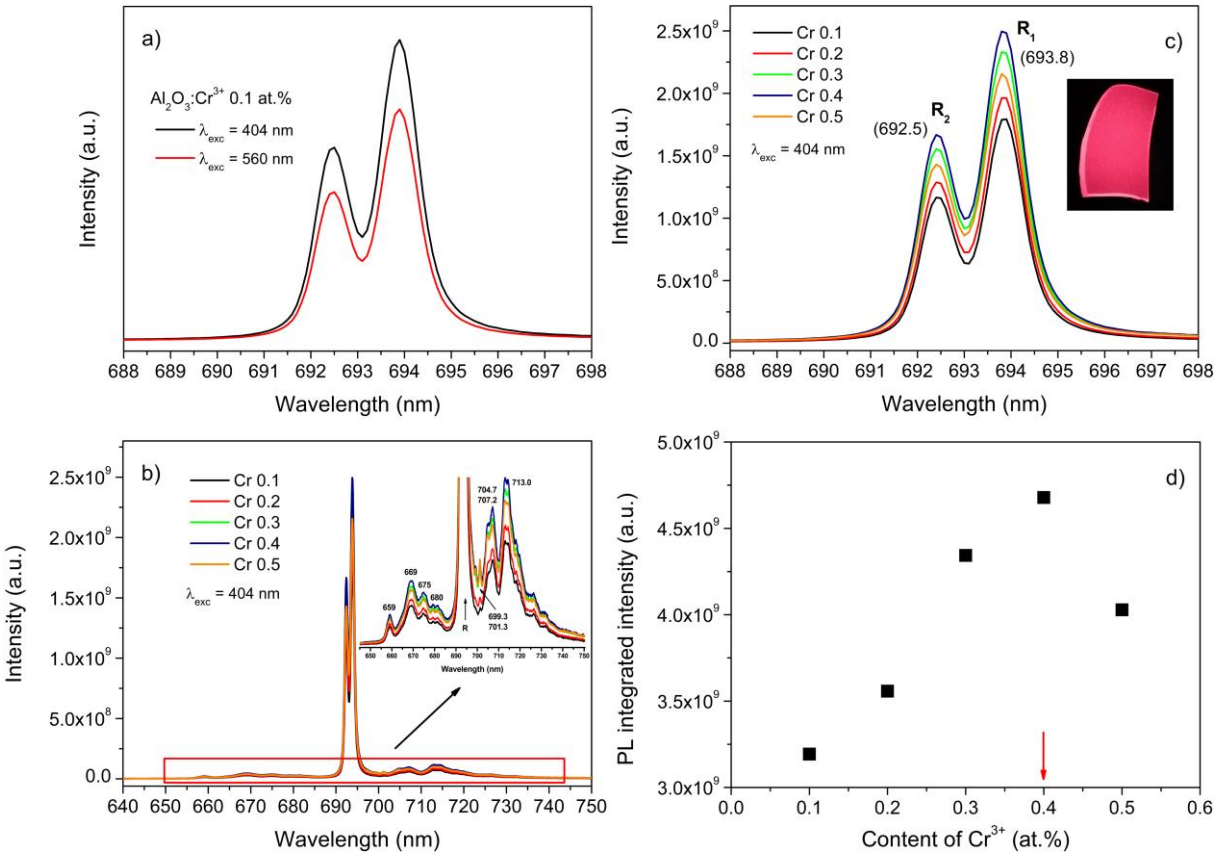
a)
$Al_2O_3:Cr^{3+}$ 0.1 at.%
$\lambda_{exc}$ = 404 nm
$\lambda_{exc}$ = 560 nm
Intensity (a.u.)
Wavelength (nm)
b)
Cr 0.1
Cr 0.2
Cr 0.3
Cr 0.4
Cr 0.5
$\lambda_{exc}$ = 404 nm
669
675
680
659
704.7
707.2
713.0
699.3
701.3
R
Wavelength (nm)
c)
$R_1$
(693.8)
$R_2$
(692.5)
d)
PL integrated intensity (a.u.)
Content of $Cr^{3+}$ (at.%)

Figure 9

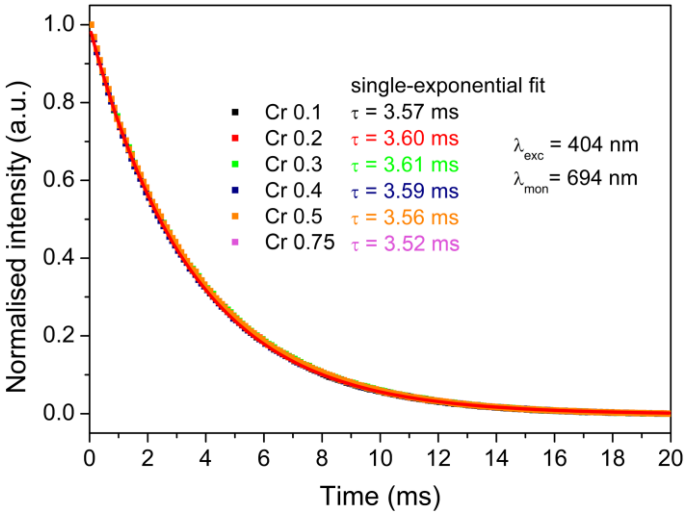
Normalised intensity (a.u.)
Time (ms)
single-exponential fit
Cr 0.1 τ = 3.57 ms
Cr 0.2 τ = 3.60 ms
Cr 0.3 τ = 3.61 ms
Cr 0.4 τ = 3.59 ms
Cr 0.5 τ = 3.56 ms
Cr 0.75 τ = 3.52 ms
λexc = 404 nm
λmon = 694 nm